Continuum model of wind-driven formation of coastal polynyas

Lailai Zhu [1,*] Bhargav Rallabandi [2] Michael Winton [3,†] and Howard A. Stone [4,‡]
[1]*Department of Mechanical Engineering, National University of Singapore 117575, Singapore*
[2]*Department of Mechanical Engineering, University of California, Riverside, California 92521, USA*
[3]*Princeton, New Jersey 08542, USA*
[4]*Department of Mechanical and Aerospace Engineering, Princeton University, Princeton, New Jersey 08544, USA*

(Received 30 May 2025; accepted 19 December 2025; published 13 February 2026)

This article is part of a Physical Review *Collection on the Physics of Changing Climate.*

Polynyas—persistent regions of open water within polar sea ice—play a critical role in polar ocean-atmosphere interactions. We combine theoretical modeling and numerical simulations to investigate the dynamics and thermodynamics of wind-driven, latent-heat-generated polynya formation adjacent to straight and curved coastlines. Under the assumption of negligible ice internal pressure, we propose a one-dimensional, continuum, mass- and momentum-conserving theory characterizing the offshore distribution of ice velocity and the spatiotemporal evolution of ice concentration. Finite-element simulations incorporating realistic sea-ice rheology validate the theoretical predictions, demonstrating strong agreement in steady-state polynya widths and ice dynamics. These results align qualitatively with observational climate data. Furthermore, we generalize the framework to two dimensions, enabling quantitative predictions of leeward polynya formation around a model circular island. The proposed theoretical framework advances mechanistic understanding of polynya formation and provides a foundation for improving their representation in climate models.

DOI: 10.1103/j24x-bf3r

I. INTRODUCTION

Polynyas—a term derived from Russian, meaning "holes of ice"—are persistent and recurrent open-water regions within polar sea ice, forming critical interfaces between ocean, atmosphere, and ecosystems [see Fig. 1(a) for examples of Antarctic polynyas]. Typically, polynyas are tens to tens of thousands of square kilometers in area [1]. Unlike the insulating sea ice cover, polynyas act as hot spots that allow the atmosphere and ocean to exchange heat, momentum, and moisture, exerting significant influences on polar climate dynamics. They also serve as "oases" for polar animals and hence are of special ecological importance [1].

According to their formation mechanism, polynyas can be categorized into sensible-heat and latent-heat types. Sensible-heat polynyas arise from thermodynamic processes, where upward heat flux from deep-ocean convection [2] or upwelling warm deep water [3] hinders ice formation and/or melts any existing ice cover. In contrast, latent-heat polynyas are mechanically driven by the wind and/or ocean currents that advect ice away from coastal barriers or edges of fast ice, as illustrated in Figs. 1(b) and 1(c). The resulting open water enhances ice production and associated brine rejection, fueling thermohaline circulation through dense water formation. Such polynyas, often called "ice factories," are most common [4].

The importance of latent-heat coastal polynyas has motivated mathematical and geophysical investigations of their formation. Two distinct approaches, the flux polynya model and the dynamic-thermodynamic sea-ice model (DTSIM), are commonly adopted. The flux model describes the polynya by its edge, where the ice concentration (or areal fraction) $c \in [0, 1]$ shifts sharply from nearly 0 (open water) to nearly 1 [5]. In particular, Lebedev [6] proposed the idea of balancing, at the edge, the ice production within the polynya and the outgoing flux of ice. One-dimensional (1D) flux polynya models were developed by Pease [7] and Ou [8] to describe the opening of an initially closed polynya that evolves in the offshore direction. The flux models proved predictive and efficient in various polynya studies [9–11]. Nevertheless, they have also been questioned for oversimplifying the physics; for example, they do not conserve momentum [12].

On the other hand, DTSIMs characterize the polynya by a continuous map of ice concentration and solve mass and momentum balance equations through direct numerical simulations (DNSs). While DTSIMs can incorporate physical processes represented by various parametrizations more easily compared to the flux polynya model, they are more computationally costly and less tractable for mechanistic understanding.

Recently, a mass- and momentum-conserving polynya flux model was developed by Morales Maqueda *et al.* [12] who introduced a jump or shock condition at the polynya edge. However, the model failed to reproduce qualitatively the

*Contact author: lailai_zhu@nus.edu.sg
†Retired.
‡Contact author: hastone@princeton.edu

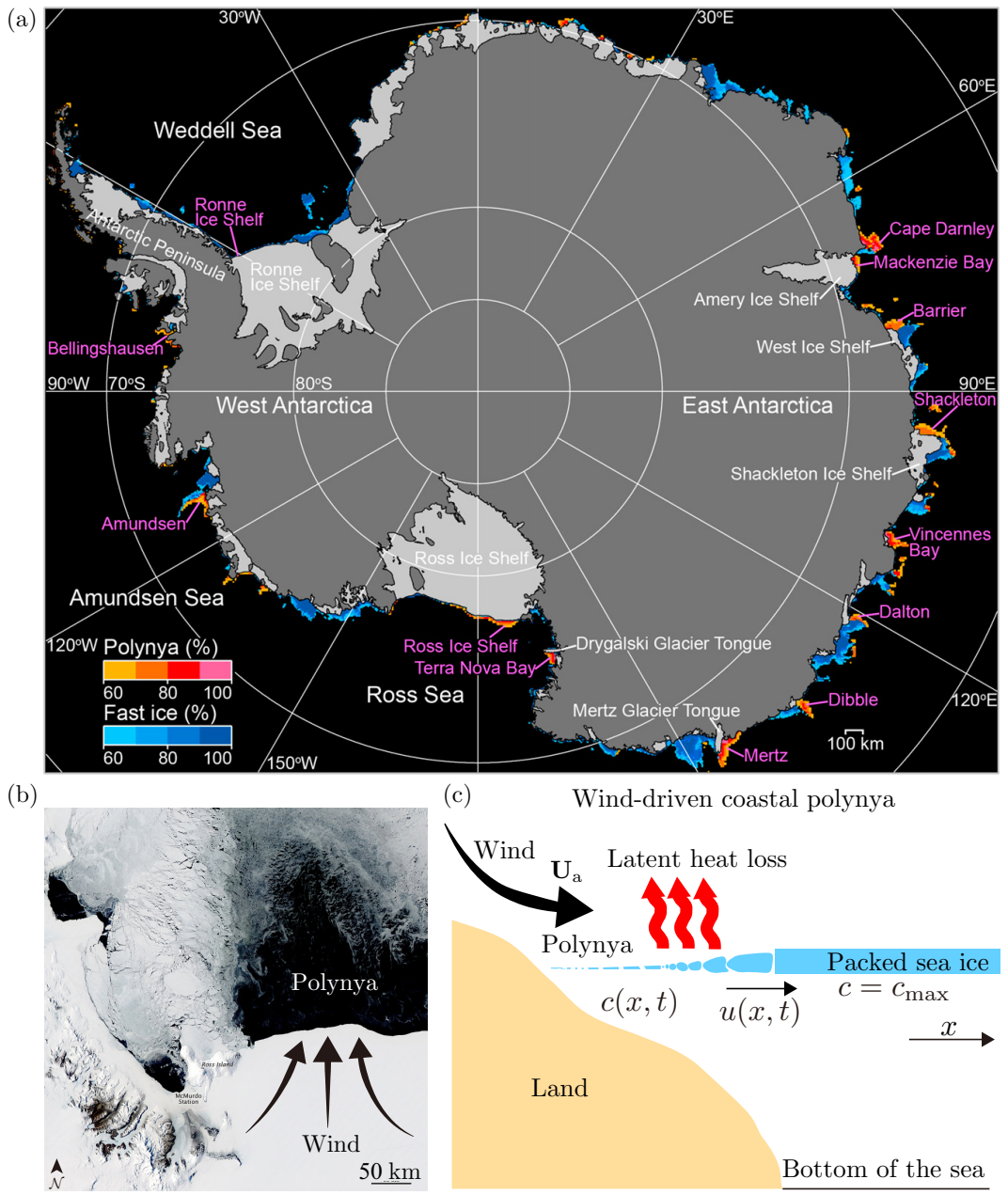

FIG. 1. Polynyas. (a) Map of Antarctic coastal polynyas, adapted from Ref. [13] with permission from © American Meteorological Society. (b) Natural-color image of the wind-driven, latent-heat coastal polynya formed near the Ross Island in the Antarctic, captured by NASA's Aqua satellite. Image is from Ref. [14]. (c) Schematic of the formation of a wind-driven, latent-heat coastal polynya.

evolution of a polynya predicted by their DNS. In this work, we develop from first principles an analytical mass- and momentum-conserving model for the opening of a wind-driven coastal polynya. We derive theoretical solutions to the governing conservation equations under simplified assumptions. Our theory demonstrates quantitative agreement with DNS results for both straight and curved coastline geometries.

The paper is organized as follows: Section II outlines the problem setup and derives the mathematical framework, followed by numerical methods and an illustrative demonstration as described in Sec. III. In Sec. IV, we present a theory for polynya dynamics, which is systematically benchmarked against DNS data in Sec. V. Finally, our findings are summarized in Sec. VI.

II. PROBLEM SETUP AND MATHEMATICAL DESCRIPTIONS

The polynya model and the DNS presented here are both based on the continuum conservation equations for ice mass and momentum. We adopt the standard momentum balance equations for sea-ice modeling, treating ice as a two-dimensional (2D) flowing continuum in the horizontal xy plane [15]. We neglect Stokes drift due to its minimal

influences at the spatiotemporal scales of polynya formation [1,12]. To maintain a reduced-physics setup, we also exclude Coriolis forces, while noting that they affect the polynya formation in general [16,17]. In addition, over the length scale of a typical polynya, the wind is regarded as steady and uniform with velocity $\mathbf{U}_a$ [8].

Denote the ice velocity by $\mathbf{u}(\mathbf{x}, t)$, where $\mathbf{x} = x\mathbf{e}_x + y\mathbf{e}_y$ and t is time. The densities of air and water are ρ_a and ρ_w, with corresponding drag coefficients C_a and C_w, respectively. Because the opening of a polynya takes a typical time of hours to days [7], inertial effects are negligible, yielding the 2D momentum equation for ice,

$$\nabla \cdot \boldsymbol{\sigma} + \boldsymbol{\tau}_a + \boldsymbol{\tau}_w = \mathbf{0}, \tag{1}$$

where $\boldsymbol{\sigma}(\mathbf{x}, t)$ is the depth-integrated (through the ice sheet) internal stress tensor, depending on ice pressure $p(\mathbf{x}, t)$, velocity $\mathbf{u}(\mathbf{x}, t)$, viscosity $\eta(\mathbf{x}, t)$, and the strain rate $\mathbf{E}(\mathbf{x}, t) = \frac{1}{2}[\nabla\mathbf{u} + (\nabla\mathbf{u})^T]$. In this context, the pressure p carries dimensions of force per unit length ($[F][L]^{-1}$), while the viscosity η is dimensionally expressed as mass per unit time ($[M][T]^{-1}$). Further, $\boldsymbol{\tau}_a = \rho_a C_a |\mathbf{U}_a| \mathbf{U}_a$ and $\boldsymbol{\tau}_w = -\rho_w C_w |\mathbf{u}| \mathbf{u}$ indicate the air and water stresses, respectively, where we have assumed quiescent ocean currents beneath the ice and zero turning angles of the air and water.

For the DNS, we implement Hibler's viscoplastic (VP) rheology [18], a widely used framework for sea-ice dynamics [19–22],

$$\boldsymbol{\sigma} = -p\mathbf{I} + \eta(\alpha^2 - 1)(\mathrm{tr}\mathbf{E})\mathbf{I} + 2\eta\mathbf{E}, \tag{2a}$$

$$p = \mathcal{P} h \exp[-k(1 - c)], \tag{2b}$$

$$\eta = \alpha^{-2} \max[p/\max(E_{\min}, E), \zeta_{\min}], \tag{2c}$$

$$E = \alpha^{-1}\sqrt{2\mathrm{tr}(\mathbf{E} : \mathbf{E}) + (\alpha^2 - 1)(\mathrm{tr}\mathbf{E})^2}, \tag{2d}$$

where α represents the yield curve eccentricity, $\mathcal{P}$ is the pressure constant for ice, $E(\mathbf{x}, t)$ is a scalar invariant of the local strain rate, and $h(\mathbf{x}, t)$ denotes ice thickness. Typical values of key parameters used in the DNS are summarized in Table I.

Regarding mass conservation for the ice sheet, we solve the coupled thermodynamic equations governing ice thickness $h(\mathbf{x}, t)$ and concentration $c(\mathbf{x}, t)$ (areal fraction),

$$h_t + \nabla \cdot (h\mathbf{u}) = S_h, \tag{3a}$$

$$c_t + \nabla \cdot (c\mathbf{u}) = S_c, \tag{3b}$$

where S_h and S_c indicate the latent-heat thermodynamic sources of thickness and concentration, respectively. Following Hibler's formulation [18], these sources are modeled as

$$S_h = (1 - c)V_f, \tag{4a}$$

$$S_c = (1 - c)V_f/h_d, \tag{4b}$$

TABLE I. Typical values of key parameters used in DNSs.

Parameters	Values
α	1.5
k	20
$\zeta_{\min}$	4×10^8 kg/s [18]
$E_{\min}$	2×10^{-9} s^{-1} [18,23]
$\mathcal{P}$	1.375×10^4 N/m^2 [24]

where $V_f = \mathcal{O}(10)$ cm/day represents the characteristic freezing rate of ice of zero thickness in winter seasons and $h_d = \mathcal{O}(1)$ m the so-called demarcation thickness. The freezing timescale t_f is defined as $t_f = h_d/V_f$. Our choice of freezing rate V_f is consistent with values adopted in previous studies, e.g., 10.5 cm/day [25], 26 cm/day [26], 27 cm/day [27], and 34 cm/day [9], as well as the observation-based estimates that report a median rate of 26 cm/day [28]. Moreover, we note that $H = h - h_d c$ satisfies the homogeneous advection equation, $H_t + \nabla \cdot (H\mathbf{u}) = 0$. Thus, H is simply advected by the flow but is unaffected by thermodynamic processes.

We clarify key assumptions underlying the simplified source terms. First, during winter, polynya water reaches below the freezing point temperature [9] and a water-air temperature difference of 20–40 °C is common [2]. This characteristic justifies considering only the latent-heat transfer but not the sensible counterpart. Moreover, we neglect heat transfer to the ocean or atmosphere where sea ice is present.

III. DIRECT NUMERICAL SIMULATIONS

We solve Eqs. (1)–(4) using the open-source library deal.II [29,30] based on the finite-element method (FEM), leveraging the approach in Ref. [31] to address the nonlinearity of the VP constitutive law. The computational domain is discretized with first-order quadrilateral elements for all the variables. The ice thickness $h(\mathbf{x}, t)$, initialized as $h(\mathbf{x}, 0) = 0.2$ m, is solved alongside concentration $c(\mathbf{x}, t)$ with an initial homogeneous field of $c(\mathbf{x}, 0) = 1$. The demarcation thickness is $h_d = 0.3$ m following Bjornsson *et al.* [25]. The adaptive mesh refinement feature of deal.II allows resolving sharp gradients in ice concentration and thickness during time evolution. Notably, the numerical tool employs body-fitted meshes for general geometries, enabling future applications to diverse sea-ice transport phenomena. The solver for reproducing our results is publicly available in Ref. [32].

Employing this solver, we simulate wind-driven polynya formation around a circular island—a configuration mirroring Arctic leeward polynyas, e.g., St. Lawrence Island, Bylot Island, or Wrangel Island. As illustrated in Fig. 2, a model circular island of radius $R_I = 80$ km is subjected to a steady rightward wind of speed $U_a = 10$ m/s and freezing rate $V_f = 15$ cm/day. Exploiting mirror symmetry, half the domain is considered. We impose zero velocity $\mathbf{u}$ along the island boundary and enforce a vanishing y component on the symmetry axis. At the leftmost boundary (i.e., the inlet), we prescribe an ice thickness $h = 0.2$ m and concentration $c = 1$, consistent with the initial state. Homogeneous Neumann conditions are applied for all other variable-boundary pairs.

Figure 2 shows the steady-state ice concentration $c(x, y)$ and velocity $\mathbf{u}(x, y)$ fields reached after ≈12 days, revealing a distinct ice-depleted wake region whose extent is comparable to the island's radius. The edge of the polynya is defined by the contour where c reaches a threshold, $\mathcal{C}_{\text{poly}}$. We set $\mathcal{C}_{\text{poly}} = 0.8$ throughout this study following Massom *et al.* [33] and Ólason and Harms [34]. Consequently, we define the polynya size L_{poly} as its extent along the centerline of the wake, reaching ≈50 km in Fig. 2.

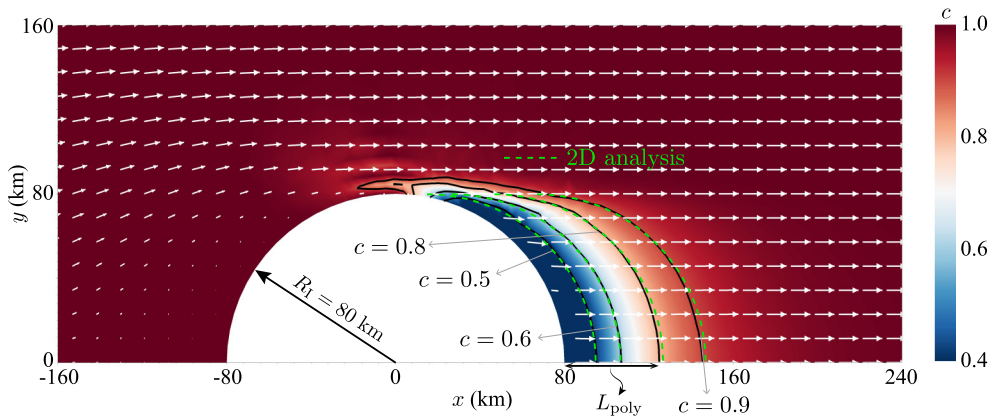

FIG. 2. FEM-based DNS shows the equilibrium ice concentration c and velocity field $\mathbf{u}$ around a circular island of radius $R_\mathrm{I} = 80\,\mathrm{km}$, where the wind velocity is $U_\mathrm{a} = 10$ m/s and $V_\mathrm{f} = 15$ cm/day. The contour line of $c = C_\mathrm{poly} = 0.8$ is identified as the edge of the polynya. The intersection between this edge and the centerline determines the polynya size, i.e., $L_\mathrm{poly} \approx 50\,\mathrm{km}$. Theoretical prediction (green dashed curves) of the contours is described in Sec. V B.

IV. THEORY

Upon observing the numerical results shown in Fig. 2, we recognize that the ice distribution does not vary significantly along the wind-normal (y) direction, especially in the leeward region adjacent to the island. This motivates an approximate 1D theoretical polynya model, neglecting the curvature of the island.

Following established flux-based models [7,8], the coastline is treated as an infinite straight no-slip boundary under offshore winds normal to the coast (Fig. 3). Because of the relatively low ice concentration inside the polynya, the internal ice pressure p, which is a measure of ice strength, is assumed to be small compared to viscous stresses. Hence, we neglect p, recovering the well-known assumption of free-drift sea ice [35–37]. The above assumptions are grounded in dimensional analysis (see Sec. VI) and further validated *a posteriori* by comparisons with the FEM-based DNS data that fully resolve ice pressure and rheology. In this framework, the internal stress reduces to

$$\boldsymbol{\sigma} = \frac{\zeta_\mathrm{min}}{\alpha^2}[2\mathbf{E} + (\alpha^2 - 1)(\mathrm{tr}\mathbf{E})\mathbf{I}]. \tag{5}$$

Consequently, the 1D momentum equation (1) is

$$\frac{(\alpha^2+1)\zeta_\mathrm{min}}{\alpha^2}\frac{\mathrm{d}^2u}{\mathrm{d}x^2} + \rho_\mathrm{a}C_\mathrm{a}{U_\mathrm{a}}^2 - \rho_\mathrm{w}C_\mathrm{w}u^2 = 0, \tag{6}$$

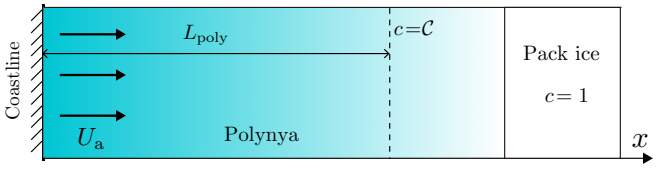

FIG. 3. Schematic of the 1D polynya model: The wind of speed U_a drags the ice away from a straight coastline. The polynya width L_poly is determined by locating the contour of $c = C_\mathrm{poly} = 0.8$.

and the 1D transport equation (3) for the concentration $c(x,t)$ is

$$\frac{\partial c}{\partial t} + \frac{\partial (uc)}{\partial x} = \frac{1-c}{t_\mathrm{f}}. \tag{7}$$

The ice concentration $c(x \to \infty, t) = 1$ signifies the pack ice region in the far field. In this theoretical framework, ice thickness h is not determined because it only influences ice transport through the internal pressure p, which is a term excluded from the momentum equation.

By setting $\mathrm{d}^2u/\mathrm{d}x^2$ to zero in Eq. (6), we obtain the free-drift velocity $U_\mathrm{d} = (\rho_\mathrm{a}C_\mathrm{a}/\rho_\mathrm{w}C_\mathrm{w})^{1/2}U_\mathrm{a}$ of the ice in the far field, $x \to \infty$, which is used as the characteristic velocity. Equation (6) describes the spatial transition of u from zero at the coastline, $x = 0$, to U_d in the far field where $\mathrm{d}^2u/\mathrm{d}x^2$ vanishes, $x \to \infty$. Notably, in FEM simulations (Sec. III), we do not prescribe the free-drift velocity U_d at the far-field boundary; instead, the numerical solution naturally converges to U_d given a sufficiently large computational domain.

Balancing the first and third terms of Eq. (6), we estimate the distance ℓ_t over which the velocity transition occurs,

$$\ell_\mathrm{t} = \left(\frac{1+\alpha^2}{\alpha^2}\right)^{1/2}\left(\frac{\zeta_\mathrm{min}^2}{\rho_\mathrm{a}\rho_\mathrm{w}C_\mathrm{a}C_\mathrm{w}U_\mathrm{a}^2}\right)^{1/4}, \tag{8}$$

which is termed the transitional length. This length ℓ_t is proportional to $U_\mathrm{a}^{-1/2}$, hence decreases with stronger winds. Besides ℓ_t, polynya formation features the freezing length scale,

$$\ell = U_\mathrm{d}t_\mathrm{f} = \left(\frac{\rho_\mathrm{a}C_\mathrm{a}}{\rho_\mathrm{w}C_\mathrm{w}}\right)^{1/2}\frac{U_\mathrm{a}h_\mathrm{d}}{V_\mathrm{f}}, \tag{9}$$

thus defining the characteristic length scale ℓ and timescale t_f in this study.

The nondimensional velocity $U = u/U_\mathrm{d}$ as a function of $X = x/\ell$ is governed by the rescaled form of Eq. (6),

$$\epsilon^2\frac{\mathrm{d}^2U}{\mathrm{d}X^2} + 1 - U^2 = 0, \tag{10}$$

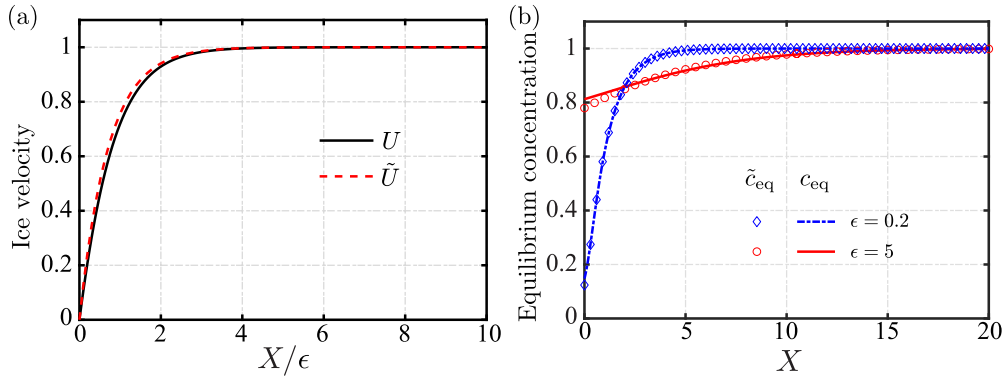

FIG. 4. Equilibrium or steady-state solutions. (a) Analytical solution [Eq. (14)] of the nondimensional equilibrium ice velocity U vs the offshore position X/ϵ (solid curve) and its approximate counterpart $\tilde{U}$ (dashed curve) [Eq. (17a)]. (b) Theoretical profile of equilibrium ice concentration $c_{eq}(X)$ obtained by numerically solving Eq. (15) along with its analytical approximate $\tilde{c}_{eq}(X)$ [Eq. (18)] when $\epsilon = 0.2$ and 5.

where

$$\epsilon = \frac{\ell_t}{\ell} = \frac{(1+\alpha^2)^{1/2}(\rho_w C_w)^{1/4} V_f \zeta_{min}^{1/2}}{\alpha(\rho_a C_a)^{3/4} U_a^{3/2} h_d} \tag{11}$$

indicates the dimensionless transitional length. Critically, ϵ characterizes the competition between freezing-caused ice formation over wind-driven ice depletion, and thus is expected to be inversely related to polynya size. Defining the dimensionless time $T = t/t_f$, the nondimensional equation (7) for $c(X,T)$ is

$$\frac{\partial c}{\partial T} + c\frac{dU}{dX} + U\frac{\partial c}{\partial X} = 1 - c \tag{12}$$

with the boundary condition $c(X \to \infty, T) = 1$ and initial condition $c(X,0) = c_0$. Here, c_0 is a constant throughout this study.

Equation (10), subject to the boundary conditions $U(X = 0) = 0$ and $U(X \to \infty) = 1$, admits the exact solution

$$X = \epsilon \int_0^{U(X)} \frac{d\lambda}{g(\lambda)}, \tag{13a}$$

where

$$g(\lambda) = \sqrt{2\lambda^3/3 - 2\lambda + 4/3}, \tag{13b}$$

along with its explicit form,

$$U(X) = 3\tanh^2\left[\frac{X}{\epsilon\sqrt{2}} + \operatorname{arctanh}\left(\sqrt{\frac{2}{3}}\right)\right] - 2. \tag{14}$$

Using $\frac{dU}{dX} = \epsilon^{-1} g(U)$ and $\frac{\partial c}{\partial X} = \frac{dU}{dX}\frac{\partial c}{\partial U}$, Eq. (12) is reformulated to

$$\frac{\partial c}{\partial T} + \epsilon^{-1}\left(U\frac{\partial c}{\partial U} + c\right) g(U) = 1 - c, \tag{15}$$

which governs $c(U(X),T)$. Based on the analytical solution (13) or (14) for $U(X)$, Eq. (15) can be solved numerically to obtain the spatiotemporal evolution $c(X,T)$. By setting $\partial c/\partial T = 0$, we further find its equilibrium distribution $c_{eq}(X)$ by numerically solving

$$\epsilon^{-1}\left(U\frac{\partial c_{eq}}{\partial U} + c_{eq}\right) g(U) = 1 - c_{eq}, \tag{16}$$

subject to $c_{eq}(U = 1) = 1$.

To gain insight into this solution, we linearize the problem around $U = 1$, equivalent to approximating $g(\lambda) \sim \sqrt{2}(1 - \lambda)$. This gives the approximate solution (indicated by $\tilde{}$) for the velocity $\tilde{U}(X)$ and ice concentration $\tilde{c}(X,T)$ as

$$\tilde{U}(X) = 1 - e^{-\sqrt{2}X/\epsilon}, \tag{17a}$$

$$\tilde{c}(X,T) = G(e^{-\sqrt{2}X/\epsilon}) - \frac{e^{\sqrt{2}X/\epsilon}\tilde{U}^{-\frac{\epsilon}{\sqrt{2}}}(e^{-\sqrt{2}T/\epsilon}\tilde{U})^{\frac{\epsilon}{\sqrt{2}}}}{e^{\sqrt{2}T/\epsilon} - \tilde{U}} \times [-1 + G[(1 - e^{-\sqrt{2}T/\epsilon}\tilde{U})^{-1}]], \tag{17b}$$

where $G(Z) = {}_2F_1(1,1;1-\epsilon/(\sqrt{2});Z)$ and ${}_2F_1(a,b;c;z)$ denotes the hypergeometric function. The corresponding equilibrium distribution of the ice concentration is

$$\tilde{c}_{eq}(X) = \frac{{}_2F_1(1,1;2+\epsilon/\sqrt{2};1-e^{-\sqrt{2}X/\epsilon})}{1+\sqrt{2}/\epsilon}. \tag{18}$$

V. THEORETICAL RESULTS COMPARED WITH NUMERICAL DATA

A. One-dimensional configuration

We first present in Fig. 4(a) the nondimensional offshore sea-ice velocity distribution, including its analytical $U(X)$ and approximate $\tilde{U}(X)$ solutions given, respectively, by Eqs. (14) and (17a). The two solutions agree well with each other, exhibiting a nearly linear variation in X/ϵ near the coast and saturating to 1 for $X/\epsilon \approx 4$. We further show the equilibrium ice distribution $c_{eq}(X)$ and $\tilde{c}_{eq}(X)$ at $\epsilon = 0.2$ and 5. The approximate solutions coincide with their analytical counterparts. As expected on physical grounds, the ice concentration evolves more gradually to the maximum value $c = 1$ at a smaller ϵ, which signifies a slower freezing rate, thus leading to a larger polynya width. The nondimensional polynya width is around 5 when $\epsilon = 0.2$. We also present the spatiotemporal evolution of the ice concentration in Fig. 5 for $\epsilon = 0.1$ and $\epsilon = 0.5$. The approximate solutions again well predict the ice distribution.

Next, we study the dimensional configurations using geophysically relevant parameters. Choosing a typical wind speed $U_a = 10$ m/s and freezing rate $V_f = 15$ cm/day, the spatiotemporal evolution of ice concentration $c(x,t)$ starting from an initial homogeneous concentration $c_0 = 1$ is displayed in

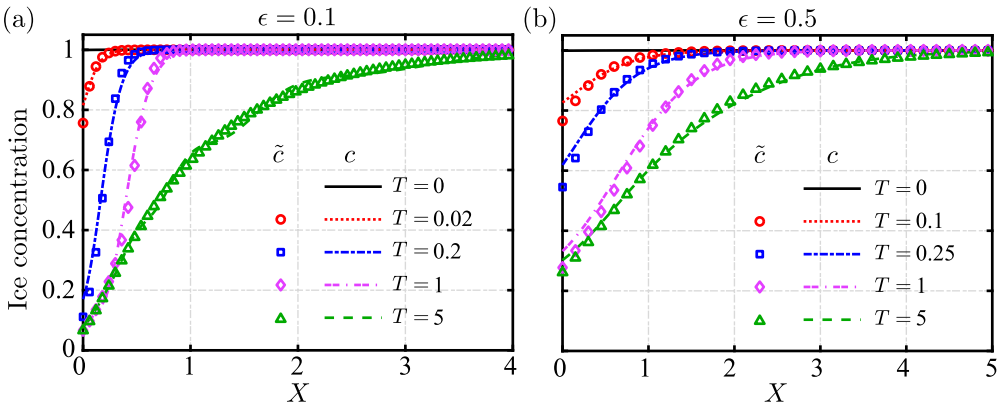

FIG. 5. Theoretical spatial-temporal evolution of ice concentration $c(X, T)$, the solution to Eq. (15), and its analytical approximate $\tilde{c}(X, T)$ [Eq. (17b)] for (a) $\epsilon = 0.1$ and (b) $\epsilon = 0.5$.

Fig. 6(a). This plot captures the polynya opening process, where the theoretical solution obtained by solving Eq. (15) aligns with the trend of DNS results but fails to resolve the steplike abrupt change of concentration in space, e.g., at $x \approx 20$ when $t = 5.6$ h and $x \approx 35$ when $t = 27.8$ h. Such jumps occur at the position at which the ice attains the free-drift velocity U_d, as depicted in Fig. 6(b). The discrepancy between theory and simulations likely stems from the increasing importance of ice rheology in the pack ice—a factor neglected theoretically. We further identify the polynya width L_{poly} by locating the contour curve $c(L_{poly}) = C_{poly} = 0.8$ (see Fig. 3). The theoretical and DNS steady-state polynya width L_{poly} as a function of U_a and V_f are shown in Fig. 7, indicating a quantitative agreement between the two datasets.

It is also noteworthy that these predictions (Fig. 7) qualitatively match the realistic polynya width that is below 100 km [33,38] (although exceptional ones such as the Okhotsk northwestern polynya can reach 300 km [26]), though we observe that when $U_a = 20$ m/s, our predictions overestimate the realistic values. We posit that the overestimation is partly attributed to our assumption that the wind is oriented orthogonal to the coast. In reality, the wind direction varies in time and is not always oriented perpendicular to the coastline; hence, the projected offshore wind speed is smaller than the measured values, resulting in a smaller polynya. Besides that, our modeling has neglected the detailed coastline geometry and ice tongues, which could also affect polynya formation. For example, the area of Mertz Glacier polynya was substantially reduced following the 2010 calving of the Mertz Glacier Tongue [39].

We present the relationship between the theoretical polynya width $L_{poly}/(\ell\epsilon)$ and ϵ^{-1}, obtained by numerically solving Eq. (16), in Fig. 8(a). All the data points collapse approximately onto a master curve, suggesting a linear relationship between the two quantities, namely, $L_{poly}/(\ell\epsilon) \sim 1/\epsilon$. In other words, $L_{poly}/\ell = \mathcal{O}(1)$ is independent of ϵ, as qualitatively revealed by Fig. 8(b) when $\epsilon \leqslant 3$. In fact, this ϵ independence holds in the limit $\epsilon \to 0$, as will be proven later.

We then take advantage of this independence and consider the limit $\epsilon \to 0$, which allows for several analytic simplifications. From Eq. (10), we see that the ice velocity is given by $U \approx 1$, except for a narrow boundary region of size $X = \mathcal{O}(\epsilon)$ [see Fig. 4(a)]. Within this region, the velocity adjusts to the boundary at $X = 0$, establishing a large velocity gradient $dU/dX = \mathcal{O}(1/\epsilon)$. The steady-state form of Eq. (12)

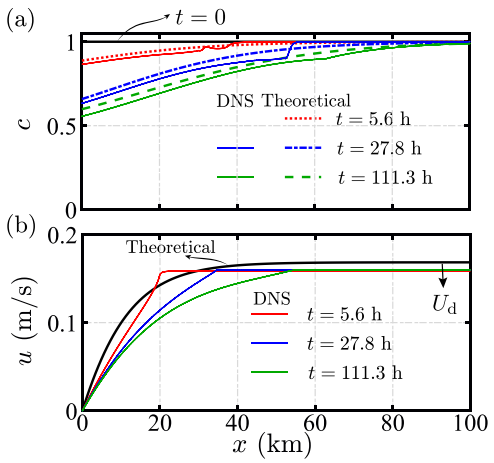

FIG. 6. Spatiotemporal evolution of (a) ice concentration $c(x, t)$ and (b) ice velocity $u(x, t)$ for $U_a = 10$ m/s and $V_f = 25$ cm/day, corresponding to $\epsilon = 1.74$. Theoretical predictions obtained by solving Eq. (15) are compared to FEM-based DNS solutions.

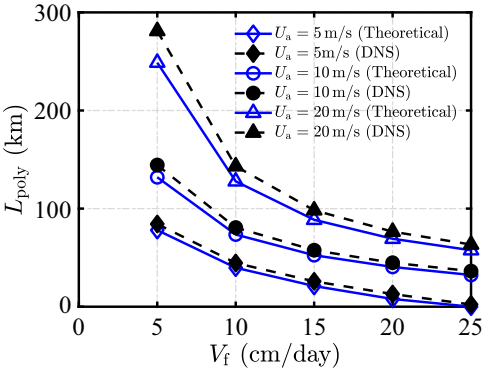

FIG. 7. Theoretical [solving Eq. (18)] and FEM-based DNS solutions of steady-state polynya width L_{poly} (km) as a function of freezing rate V_f at wind speeds of $U_a = 5$ m/s (diamonds), 10 m/s (circles), and 20 m/s (triangles).

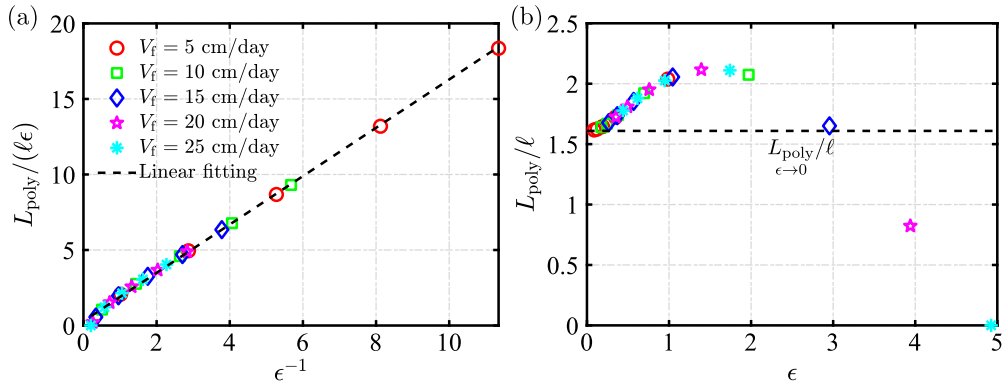

FIG. 8. Polynya widths for different parameter values. (a) Theoretical polynya width $L_{poly}/(\ell\epsilon)$ vs ϵ^{-1} at various freezing rates V_f, obtained by solving Eq. (18). (b) L_{poly}/ℓ as a function of ϵ, in comparison to the limiting formula [Eq. (20)] derived in the limit $\epsilon \to 0$.

when evaluated at $X = 0$ yields the boundary condition $c = 1/(1 + dU/dX)$, which is approximately zero due to the large velocity gradient at $X = 0$. Outside of the thin region, $U \approx 1$ and $dU/dX \approx 0$, so that Eq. (12) reduces to $dc/dX = 1 - c$. This yields an approximate solution at steady state,

$$c(X) \approx 1 - e^{-X}, \quad \epsilon \to 0 \quad \text{(steady state)}. \tag{19}$$

The extent of the polynya is identified by $c = \mathcal{C}_{poly}$, corresponding to $X = \ln(\frac{1}{1-\mathcal{C}_{poly}})$. Given the definition of ℓ in Eq. (9), we deduce the polynya width in the limit $\epsilon \to 0$:

$$\begin{aligned} \underset{\epsilon\to 0}{L_{poly}} &= \ln\left(\frac{1}{1-\mathcal{C}_{poly}}\right)\ell \\ &= \frac{U_a h_d}{V_f}\left(\frac{\rho_a C_a}{\rho_w C_w}\right)^{1/2} \ln\left(\frac{1}{1-\mathcal{C}_{poly}}\right). \end{aligned} \tag{20}$$

This prediction shows that the steady-state polynya width exhibits a linear scaling with wind speed U_a and inverse proportionality to the freezing rate V_f, while displaying a comparatively mild dependence on $\mathcal{C}_{poly}$. Despite its simplicity, the limiting formula (20) reasonably approximates the theoretical solutions as indicated in Fig. 8(b), particularly for small ϵ. Furthermore, as evidenced in Fig. 9, these theoretical solutions, FEM-based DNS results, and Eq. (20) all exhibit a generally close alignment.

B. Two-dimensional analysis

Using the insights gained from the 1D theory, we develop its 2D variant to describe the steady-state polynya formed at the leeside of potentially curved coastlines. We consider a coastal boundary $\mathcal{B}$ described by a general shape profile, $X = X_{\mathcal{B}}(Y)$. As in the DNS, we orient the x axis along the wind direction (cf. Fig. 2). We expect the ice velocity to also be directed primarily along x, but may vary with both x and y to conform to conditions on the coastline, i.e., $\mathbf{u} = u(x, y)\mathbf{e}_x$. The concentration field also now depends on x and y for the same reasons.

We again focus on the asymptotic limit $\epsilon \to 0$. The velocity remains approximately constant, $U \approx 1$, except within a narrow boundary layer of width ϵ on the leeward side of the coastline. As before, the ice concentration approaches 1 exponentially; however, the boundary condition $c = 0$ is here satisfied along the curve $X = X_{\mathcal{B}}(Y)$ describing the coastal shape. Invoking the same arguments as with the 1D analysis, the steady-state concentration profile is

$$c(X, Y) = 1 - \exp\{-(X - X_{\mathcal{B}}(Y))\}, \tag{21}$$

which depends on the shape of the boundary. Based on Eq. (21), we obtain an equation for the contour line with a constant C,

$$X = X_{\mathcal{B}}(Y) + \ln\left(\frac{1}{1-C}\right). \tag{22}$$

Notably, the contour corresponding to C is a leeward shift of the coastal profile by a distance of $\ln(\frac{1}{1-C})$. The width of the polynya is constant as measured from the coastline in the along-wind direction, and is given by Eq. (20).

The model circular island illustrated in Sec. III is described by the shape $X_{\mathcal{B}} = \sqrt{(R_I/\ell)^2 - (Y)^2}$. Then, Eq. (21) yields a prediction for the steady-state spatial distribution of ice concentration $c(X, Y)$. Contours of this theoretical prediction (green dashed lines) are in excellent agreement with the numerical counterpart that includes ice rheology, as shown in Fig. 2.

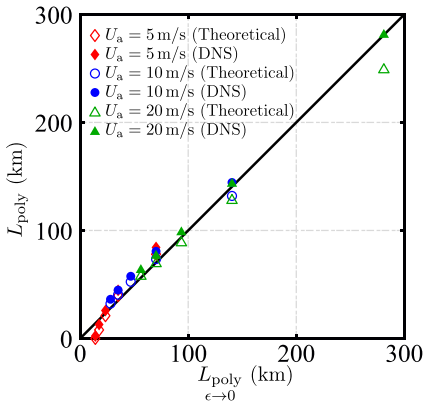

FIG. 9. Theoretical steady-state polynya width L_{poly} (km) obtained through Eq. (18) and the FEM-based solutions in comparison with $\underset{\epsilon\to 0}{L_{poly}}$ [Eq. (20)] at a wind speed of $U_a = 5$ m/s (diamonds), 10 m/s (circles), and 20 m/s (triangles).

VI. CONCLUSIONS AND DISCUSSIONS

Polynyas are pivotal features in polar oceanography, acting as critical sites for ocean-atmosphere exchange and ice production. Understanding their formation mechanisms is essential for improving climate models and predicting long-term changes in polar environments. In this study, we developed a theoretical framework to predict wind-driven latent-heat polynya dynamics along coastlines and islands, neglecting the internal pressure and rheology of the sea ice. The theoretical model is governed by the dimensionless parameter ϵ, which quantifies the ratio of freezing-caused ice formation to wind-driven ice depletion. To benchmark the theory, we have also conducted DNSs based on a finite-element method to solve the dynamics of ice considering its full rheology.

We first consider a steady and uniform wind directed normal to a straight coastline, enabling a 1D theoretical framework. We derive theoretical solutions for the steady velocity distribution and the spatiotemporal evolution of ice concentration offshore. By invoking a linearization, the solutions are further simplified into a closed-form expression. Applying this model to a geophysically relevant configuration, we find that the theoretically predicted spatiotemporal evolution of ice concentration captures the general trend observed in DNS results but fails to resolve abrupt spatial gradients in concentration. This failure mostly results from the neglect of ice rheology in the theoretical formulation. Nevertheless, the theoretical polynya width L_{poly} quantitatively agrees with its numerical counterpart across a wide range of wind speeds and ice freezing rates. Moreover, the weak dependence of L_{poly} on ϵ prompts an analysis in the limit $\epsilon \to 0$. This leads to a simple limiting formula [Eq. (20)] for polynya width, which linearly scales with the wind speed, demarcation thickness, and the inverse of freezing rate.

Considering the same limit $\epsilon \to 0$, we generalize the 1D theory for a straight coastline into a 2D variant that accommodates arbitrarily shaped coastlines. It provides a closed-form solution for the 2D spatial distribution of ice concentration, its contour lines, and the polynya width. The 2D theoretical predictions agree well with DNS data, as demonstrated in the case of polynya formation near a circular island.

Finally, we note that within a polynya, the ratio of pressure p to viscous stresses exhibits a characteristic upper bound (considering $c \leqslant \mathcal{C}_{\text{poly}}$), $\mathcal{P}h \exp[-k(1-\mathcal{C}_{\text{poly}})]h_{\text{d}}/V_{\text{f}} \approx 0.16$. This bound corroborates our theoretical assumption (see Sec. IV); namely, the pressure remains secondary to viscous stress in the polynya.

In summary, this work provides a theoretical framework elucidating the dynamics of wind-driven coastal polynya formation. Our findings advance the mechanistic understanding of this process and could enhance its parametrization in climate models, thereby offering a pathway to improve predictions of polar climate feedbacks.

ACKNOWLEDGMENTS

L.Z. acknowledges the partial support received from the National University of Singapore, under the startup Grant No. A-0009063-00-00. B.R. thanks the Hellman Foundation for partial support. H.A.S. thanks the NSF for support via Grant No. CBET-2246791. The Carbon Mitigation Initiative of Princeton University is acknowledged for the partial support of this research. Computation of the work was performed on resources of the National Supercomputing Centre, Singapore [40], as well as those provided by NUS IT via Grant No. NUSREC-HPC-00001.

DATA AVAILABILITY

The data supporting this study's findings are available within the article.

[1] W. O. Smith Jr. and D. G. Barber, *Polynyas: Windows to the World* (Elsevier Science Inc., New York, 2007), Vol. 74.

[2] S. D. Smith, R. D. Muench, and C. H. Pease, Polynyas and leads: An overview of physical processes and environment, J. Geophys. Res. **95**, 9461 (1990).

[3] J. C. Comiso and A. L. Gordon, Cosmonaut polynya in the Southern Ocean: Structure and variability, J. Geophys. Res. **101**, 18297 (1996).

[4] W. J. Williams, E. C. Carmack, and R. G. Ingram, Physical oceanography of polynyas, Elsevier Oceanogr. Ser. **74**, 55 (2007).

[5] A. J. Willmott, D. M. Holland, and M. A. Morales Maqueda, Polynya modelling, Elsevier Oceanogr. Ser. **74**, 87 (2007).

[6] V. L. Lebedev, Maximum size of a wind-generated lead during sea freezing, Oceanology **8**, 313 (1968).

[7] C. H. Pease, The size of wind-driven coastal polynyas, J. Geophys. Res. **92**7049 (1987).

[8] H. W. Ou, A time-dependent model of a coastal polynya, J. Phys. Oceanogr. **18**, 584 (1988).

[9] M. A. Morales Maqueda, A. J. Willmott, and N. R. T. Biggs, Polynya dynamics: A review of observations and modeling, Rev. Geophys. **42**, RG1004 (2004).

[10] N. R. T. Biggs and A. J. Willmott, Unsteady polynya flux model solutions incorporating a for the collection thickness of consolidated new ice, Ocean Modell. **7**, 343 (2004).

[11] I. A. Walkington and A. J. Willmott, A coupled coastal polynya–atmospheric boundary layer model, J. Phys. Oceanogr. **36**, 897 (2006).

[12] M. A. Morales Maqueda, A. J. Willmott, and I. A. Walkington, The opening of wind-driven polynyas, J. Fluid Mech. **746**, 236 (2014).

[13] S. Nihashi and K. I. Ohshima, Circumpolar mapping of Antarctic coastal polynyas and landfast sea ice: Relationship and variability, J. Clim. **28**, 3650 (2015).

[14] https://earthobservatory.nasa.gov

[15] M. D. Coon, G. A. Maykut, and R. S. Pritchard, Modeling the pack ice as an elastic-plastic material, AIDJEX Bull. **4**, 1 (1974).

[16] A. M. J. Davis and R. T. McNider, The development of Antarctic katabatic winds and implications for the coastal ocean, J. Atmos. Sci. **54**, 1248 (1997).

[17] Y. Xu, W. Zhang, T. Maksym, R. Ji, and Y. Li, Stratification breakdown in Antarctic coastal polynyas. Part I: Influence

of physical factors on the destratification time scale, J. Phys. Oceanogr. **53**, 2047 (2023).
[18] W. D. Hibler III, A dynamic thermodynamic sea ice model, J. Phys. Oceanogr. **9**, 815 (1979).
[19] C. Gordon, C. Cooper, C. A. Senior, H. Banks, J. M. Gregory, T. C. Johns, J. F. B. Mitchell, and R. A. Wood, The simulation of SST, sea ice extents and ocean heat transports in a version of the Hadley coupled model without flux adjustments, Clim. Dyn. **16**, 147 (2000).
[20] P. Wadhams, *Ice in the Ocean* (CRC Press, Boca Raton, Florida, 2014).
[21] B. Rallabandi, Z. Zheng, M. Winton, and H. A. Stone, Wind-driven formation of ice bridges in straits, Phys. Rev. Lett. **118**, 128701 (2017).
[22] B. Rallabandi, Z. Zheng, M. Winton, and H. A. Stone, Formation of sea ice bridges in narrow straits in response to wind and water stresses, J. Geophys. Res. C: Oceans **122**, 5588 (2017).
[23] E. C. Hunke, Viscous–plastic sea ice dynamics with the EVP model: Linearization issues, J. Comput. Phys. **170**, 18 (2001).
[24] W. D. Hibler III, and S. F. Ackley, Numerical simulation of the Weddell Sea pack ice, J. Geophys. Res. **88**, 2873 (1983).
[25] H. Bjornsson, A. J. Willmott, L. A. Mysak, and M. A. Morales Maqueda, Polynyas in a high-resolution dynamic–thermodynamic sea ice model and their using flux models, Tellus A **53**, 245 (2001).
[26] Y. Kawaguchi, S. Nihashi, H. Mitsudera, and K. I. Ohshima, Formation mechanism of huge coastal polynyas and its application to Okhotsk northwestern polynya, J. Phys. Oceanogr. **40**, 2451 (2010).
[27] M. A. Morales Maqueda and A. J. Willmott, A two-dimensional time-dependent model of a wind-driven coastal polynya: Application to the St. Lawrence Island polynya, J. Phys. Oceanogr. **30**, 1281 (2000).
[28] S. F. Ackley, S. Stammerjohn, T. Maksym, M. Smith, J. Cassano, P. Guest, J.-L. Tison, B. Delille, B. Loose, P. Sedwick, *et al.*, Sea-ice production and air/ice/ocean/biogeochemistry interactions in the Ross Sea during the PIPERS 2017 autumn field campaign, Ann. Glaciol. **61**, 181 (2020).
[29] G. Alzetta, D. Arndt, W. Bangerth, V. Boddu, B. Brands, D. Davydov, R. Gassmoeller, T. Heister, L. Heltai, K. Kormann, M. Kronbichler, M. Maier, J.-P. Pelteret, B. Turcksin, and D. Wells, The deal.II library, version 9.0, J. Numer. Math. **26**, 173 (2018).
[30] W. Bangerth, R. Hartmann, and G. Kanschat, Deal.II—A general purpose object oriented finite element library, ACM Trans. Math. Softw. **33**, 24/1 (2007).
[31] J. Zhang, and W. D. Hibler III, On an efficient numerical method for modeling sea ice dynamics, J. Geophys. Res. **102**, 8691 (1997).
[32] https://github.com/lailaiflow/sea_ice_simulation_FEM
[33] R. A. Massom, P. T. Harris, K. J. Michael, and M. J. Potter, The distribution and formative processes of latent-heat polynyas in East Antarctica, Ann. Glaciol. **27**, 420 (1998).
[34] E. Ólason and I. Harms, Polynyas in a dynamic-thermodynamic sea-ice model, The Cryosphere **4**, 147 (2010).
[35] M. G. McPhee, An analysis of pack ice drift in summer, in *Sea Ice Processes and Models*, edited by R. S. Pritchard (University of Washington Press, WA, 1980), Vol. 1, p. 62.
[36] M. Leppäranta and A. Omstedt, Dynamic coupling of sea ice and water for an ice field with free boundaries, Tellus A **42**, 482 (1990).
[37] M. Leppäranta, *The Drift of Sea Ice* (Springer Science & Business Media, Berlin, Heidelberg, 2011).
[38] R. G. Barry, M. C. Serreze, J. A. Maslanik, and R. H. Preller, The Arctic sea ice-climate system: Observations and modeling, Rev. Geophys. **31**, 397 (1993).
[39] M. Lacarra, M.-N. Houssais, C. Herbaut, E. Sultan, and M. Beauverger, Dense shelf water production in the Adélie Depression, East Antarctica, 2004–2012: Impact of the Mertz Glacier calving, JGR Oceans **119**, 5203 (2014).
[40] https://www.nscc.sg